

# Microplastic Identification via Holographic Imaging and Machine Learning

Vittorio Bianco, Pasquale Memmolo, Pierluigi Carcagnì, Francesco Merola, Melania Paturzo, Cosimo Distante, and Pietro Ferraro\*

Microplastics (MPs) are a major environmental concern due to their possible impact on water pollution, wildlife, and the food chain. Reliable, rapid, and high-throughput screening of MPs from other components of a water sample after sieving and/or digestion is still a highly desirable goal to avoid cumbersome visual analysis by expert users under the optical microscope. Here, a new approach is presented that combines 3D coherent imaging with machine learning (ML) to achieve accurate and automatic detection of MPs in filtered water samples in a wide range at microscale. The water pretreatment process eliminates sediments and aggregates that fall out of the analyzed range. However, it is still necessary to clearly distinguish MPs from marine microalgae. Here, it is shown that, by defining a novel set of distinctive “holographic features,” it is possible to accurately identify MPs within the defined analysis range. The process is specifically tailored for characterizing the MPs’ “holographic signatures,” thus boosting the classification performance and reaching accuracy higher than 99% in classifying thousands of items. The ML approach in conjunction with holographic coherent imaging is able to identify MPs independently from their morphology, size, and different types of plastic materials.

The term microplastics (MPs) refers to plastic material with diameter lower than 5 mm. Mostly, MPs are generated from breakup of larger items or mass produced to match industrial and market needs.<sup>[3,4]</sup> Wastewater treatment plants are an important hub of MP pollutants as well, and their direct release to the environment needs to be continuously monitored.<sup>[5,6]</sup> However, reliable identification of MPs in water is still a challenging ambition and thus highly demanded to map and understand their impact on human health as well as marine economic activities.<sup>[2,7]</sup> There are major concerns that ingestion of MPs by marine organisms could lead to toxicological harm.<sup>[8–10]</sup> MPs can occur in high abundances at the sea surface, in the water column, and on the seabed, including the deep sea. Studies have recently detected MPs in freshwater sources and drinking water, alerting us about potential threats for human health.<sup>[11]</sup> Despite these concerns about MPs, protocols for sampling

## 1. Introduction


The largest percentage of marine litter consists of plastic wastes, the biodegradation process of which can take decades to complete.<sup>[1,2]</sup> The main concerns about the negative effects of plastics in a marine environment are related to the severe impact that such small particles have on wildlife and finally on humans.

campaigns and classification methods are not well assessed yet.<sup>[3,10,11]</sup> So far, analytical methods for identifying and counting MPs are still only at a basic developing stage, although research about MPs is a vast emerging field.<sup>[12]</sup> Typically, analytical procedures for MP identification in environmental samples consist of multiple steps, i.e., extraction, isolation, identification, and classification. As long as the sizes of MPs stay in the range 1–5 mm, visual sorting by expert users has been adopted for detecting them. Therefore, an automated and robust identification and counting method is highly demanded to perform effective ecological risk assessment, especially at micrometer scales.<sup>[12]</sup> Indeed, under 1 mm, the identification of each single object inside a pretreated water sample is usually made by unaided eyes at the optical microscope. Pretreatment steps usually include digestion, sieving, or filtration of natural water to exclude sediments falling outside the analysis range and to avoid coating of MPs by bacteria biofilm or marine algae.

Basically, common approaches to identify MPs are based on the combination of two analytical techniques, i.e., their physical characterization, using optical microscopes, followed by their chemical characterization through spectroscopy methods for assessing the plastic type.<sup>[13–16]</sup> Stereomicroscopy is the most used method to identify MPs in the range 0.1–1 mm of sizes,<sup>[17]</sup> whereas scanning electron microscopy (SEM) can identify

Dr. V. Bianco, Dr. P. Memmolo, Dr. F. Merola, Dr. M. Paturzo, Dr. P. Ferraro  
Institute of Applied Sciences and Intelligent Systems (ISASI)  
National Research Council (CNR) of Italy  
Via Campi Flegrei 34, 80078 Pozzuoli, NA, Italy  
E-mail: p.ferraro@isasi.cnr.it

Dr. P. Carcagnì, Dr. C. Distante  
Institute of Applied Sciences and Intelligent Systems (ISASI)  
National Research Council (CNR) of Italy  
Via Monteboni snc University Campus, 73100 Lecce, Italy

 The ORCID identification number(s) for the author(s) of this article can be found under <https://doi.org/10.1002/aisy.201900153>.

© 2020 The Authors. Published by WILEY-VCH Verlag GmbH & Co. KGaA, Weinheim. This is an open access article under the terms of the Creative Commons Attribution License, which permits use, distribution and reproduction in any medium, provided the original work is properly cited.

DOI: 10.1002/aisy.201900153

plastic-like particles under 0.1 mm.<sup>[18]</sup> Fluorescence microscopy, atomic force microscopy, and polarized microscopy have been used to identify specific classes of MPs.<sup>[12]</sup> All these methods are intrinsically low throughput, time consuming, and not deployable in situ for continuous and/or rapid monitoring. A processing protocol for rapid and automatic MP recognition is still missing.

Recently, digital holography (DH) has been used to image MPs, demonstrating its preliminary potential use for the physical characterization of plastic-like particles.<sup>[19,20]</sup>

DH can provide useful capabilities such as label-free 3D imaging, flexible focusing of samples in microfluidic streams, and high throughput. In addition, DH technology is mature to provide low-cost field-portable systems for in situ environmental monitoring.<sup>[21,22]</sup>

Here we show a novel approach, named holographic plastics identification (HPI), which combines DH with artificial intelligence to achieve very accurate identification of MPs inside heterogeneous pretreated water samples. We used a machine learning (ML) paradigm relying on features extracted from holographic images and used as the input of a well-established support vector machine (SVM).<sup>[23]</sup> We refer to this combination as “holographic SVM” (H-SVM), having in mind that the HPI is a more general paradigm and in principle different classifiers could be embedded instead of the SVM.

Bucking the main trend of deep learning for image classification in microscopy,<sup>[24–27]</sup> we show that the coherent nature of holographic imaging in microscope configuration permits us to extract such a rich information content that more complex artificial intelligence schemes are not necessary for this scope. Therefore, we demonstrate that it is possible to determine an optimal set of “holographic features” extracted from the digital holograms, with the scope of identifying a distinctive marker for the MP class. Thus, these can be thought of as a specific “fingerprint” for the whole MP population.

Automatic recognition of MPs in a heterogeneous mix is an ambitious goal, as marine water samples include organisms sharing with plastics the same wide range of characteristic scales, due to the abundant presence of plankton and nekton. In

particular, we have identified marine diatoms,<sup>[28]</sup> i.e., a population of microorganisms belonging to the phytoplankton group, as one of the most problematic classes of micro-objects that can be easily confused with MPs, thus impairing automatic recognition by optical microscopes even after pretreatment of natural water.

The methodology we propose can recognize MPs and is over 99% accurate<sup>[29]</sup> in discriminating them from diatoms in the presence of a wide heterogeneity of sizes, shapes, and plastic material types. The proposed method could be the first step to automatize the MP identification procedure and to make it reliable by significantly augmenting the number of objects analyzed. The aim of this work is to provide an automatic prescreening tool that could replace unaided microscope observation of pretreated water samples.

## 2. Working Principle

We consider ten populations of micro-objects (i.e., nine diatom species [DS] and a heterogeneous mix of MPs, with size < 1 mm) to be imaged in our holographic microscope, and we implement a fully automatic pipeline to detect and classify MPs. The heterogeneous mix of MPs consists of different types of materials such as polystyrene (PS), polyethylene (PE), polypropylene (PP), polyvinylchloride (PVC), and PE terephthalate (PET) (see Supporting Information for further details). The DS we analyzed will be hereafter indicated with DS1,...,DS9. The corresponding species names are shown in **Figure 1** along with the area intervals where each species is distributed. The sizes of the MPs constituting the sample under test vary uniformly in the chosen analysis range, i.e., 20 μm to 1 mm, while each DS provides a classical Gaussian statistical distribution. We limited our analysis to this range of sizes as larger items are more easily identifiable and can be excluded from the liquid sample by net water filters during the sampling operations.<sup>[12]</sup> To show the set of populations to be classified, we selected for illustrative purposes just one element per class and we have shown in Figure 1 the corresponding modulus-2π phase images after refocusing. From the area intervals shown in Figure 1, it can be inferred that MP areas are

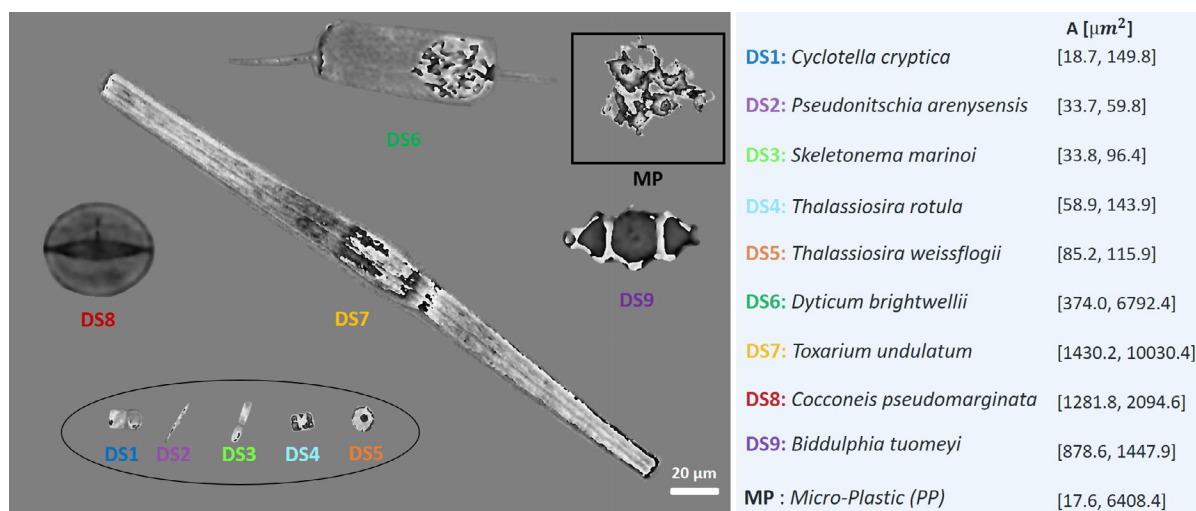


**Figure 1.** Complexity of the MP identification problem. Synthetic image reporting the wrapped phase maps of one element per DS and a typical MP (in the black box). The species/type names are reported on the right side along with the area intervals, A, where each population is distributed.

spread over the entire region where the other classes are distributed, in part or entirely.

The physical principle that governs the adopted imaging method is the theory of scalar diffraction, which is well established and used to model phenomena of light diffraction and propagation from objects of known regular shape. The DH principle and imaging method derive from that and is able to recover the diffracted wavefront signature of an object probed by coherent light. Here we relied on a machine learning (ML) approach to accurately identify MPs, as developing a model of diffraction from these very complex objects would be an unfeasible task due to the large heterogeneity of MPs in terms of shapes, sizes, and attitudes to interact with the light beam.

After recording digital holograms of the samples, we apply holographic object detection and automatic refocusing to reconstruct the complex wavefronts of each object in the field of view (FoV).<sup>[30]</sup> Then, we extract the modulus- $2\pi$  or “wrapped” phase images, from which we segment the detected objects. Details of the proposed processing pipeline are reported in the following.

### 2.1. Holographic Recording and Reconstruction

We performed several experiments for recording holographic data of each population. For each experiment, a drop of seawater

containing MPs and/or diatoms was imaged under the holographic microscope. The experimental setup is shown in **Figure 2a** and described in detail in the Supporting Information. The HPI processing pipeline is shown in **Figure 2b**. This can be conceptually thought of as made up of three parts. The first is devoted to detect the objects inside the FoV and reconstruct the complex object in sharp focus. The second extrapolates the complete set of features from the object complex information. These have to be informative enough to take into account the large heterogeneity of the MP population, in terms of shapes, sizes, and compositions of the materials involved and thus light absorption properties. Actually, over 90% of them are made of PE, PP, PET, nylon, PMMA, PS, and PVC aggregated in clusters of various sizes.<sup>[31,32]</sup> Optical microscope photographs of the MPs belonging to the mix used in our experiments are shown in **Figure 2c** and show their large heterogeneity on different scales.

The last block uses the feature set to classify the objects and is described in detail in the Supporting Information. Let  $H$  be the hologram recorded in off-axis configuration in transmission geometry, and let  $H_F$  be the corresponding complex image after demodulation and selection in the Fourier domain of the first order of diffraction.<sup>[33]</sup> Then, a first stage of segmentation provides the estimate of the centroid of each object. Once the

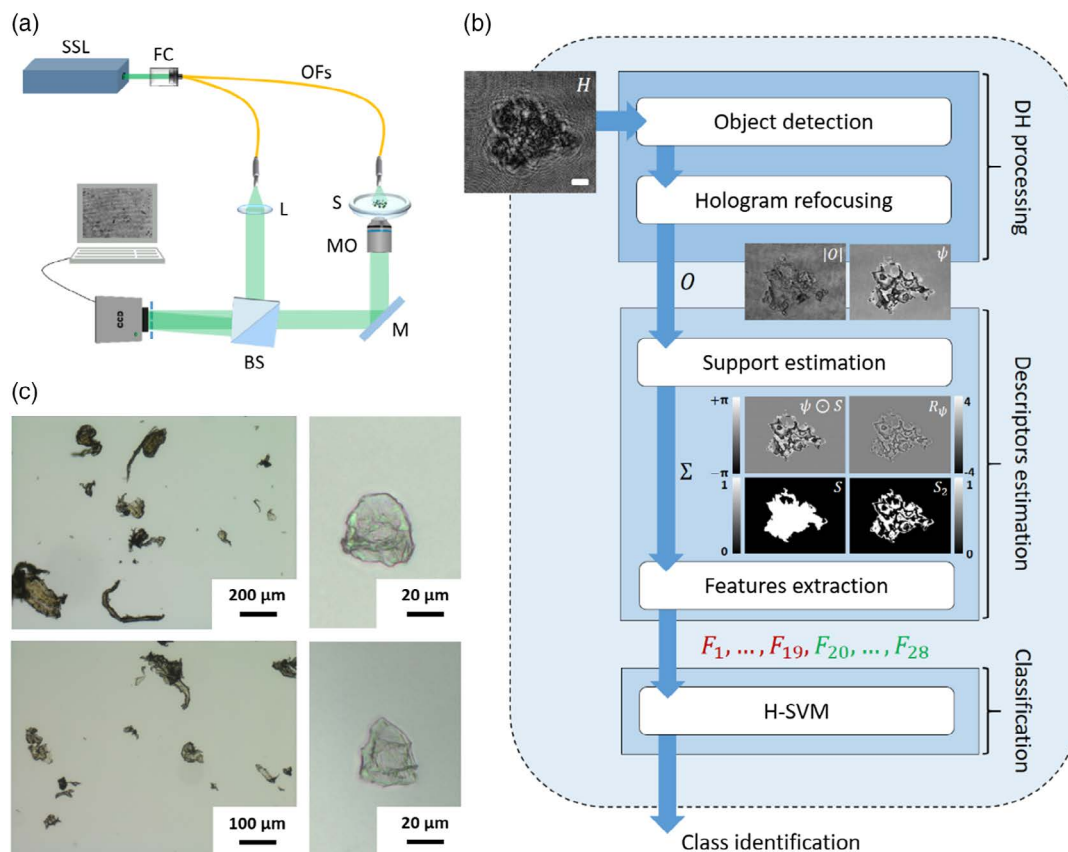


**Figure 2.** HPI. a) Sketch of the experimental setup used for sample recording. SSL, solid state laser; FC, fiber coupler; OF, optical fiber; S, sample; L, lens; MO, microscope objective; M, mirror; BS, beam splitter; CCD, charge coupled device. b) Image processing pipeline used to reconstruct the DHs, extract the features, and accomplish the classification task (scale bar: 5  $\mu$ m). c) Optical microscope photographs of various MPs belonging to the mix used in our experiments.

centroid of an object is localized, automatic focusing yields its best focus distance,  $z_F$ . This is trivially obtainable by optimization of the proper contrast metrics, e.g., the Tamura coefficient or the Tamura of gradient operators.<sup>[34]</sup> Numerical propagation returns the complex object  $O = A_S\{H_F; z_F\}$ , where  $A_S\{\dots\}$  denotes the angular spectrum propagation operator.<sup>[33]</sup> Extracting the amplitude pattern from the complex object is not the best choice when MP samples are imaged. Depending on the plastic type, for any fixed visible wavelength of the probing beam, these are characterized by different absorption characteristics, some of them behaving as highly absorbing samples, others as almost transparent objects. For this reason, any classification method based on the sole amplitude or intensity pattern would fail. Instead, we extract the modulus- $2\pi$ , or “wrapped” phase contrast,  $\psi = \text{Angle}\{O/C_R\}$ , where we denote with  $C_R = A_S\{H_{F-R}; z_F\}$  the reconstruction at distance  $z_F$  of a demodulated reference hologram,  $H_{F-R}$ , used to compensate the wavefront aberrations introduced by the optics in the setup. This procedure is repeated for all diatoms and MPs.

## 2.2. Holographic Feature Extraction

Examples of MPs extracted from the reconstructed population are shown in **Figure 3a**, where their modulus- $2\pi$  phase-contrast images are reported and sorted by area. The large scales and shape variability of MPs make arduous their classification from DS by looking at the sole morphological parameters. Therefore, a more distinctive set of features needs to be defined.

In DH, to measure the sample optical thickness, phase unwrapping is usually operated.<sup>[35]</sup> However, we noted that the structure of the MP samples provokes sudden phase jumps that make the unwrapping procedure unfeasible or not reliable enough for most of the objects. The large spatial density of the phase jumps in the wrapped phase-contrast map of MPs has not been recognized in natural objects such as algae of comparable size.<sup>[36,37]</sup>

Although this is generally a drawback for imaging the samples, we believe it is an opportunity for the purpose of classification. Indeed, the high spatial density of the phase jumps in the wrapped phase-contrast map could be a distinctive feature for the wide MP class.

We use  $\psi$  to extract the complete set of descriptors we rely on (see Supporting Information). Let  $F_i$  ( $i = 1, \dots, 28$ ) be the features we extract. These are calculated from a set of four maps

$$\Sigma = [\psi; R_\psi; S; S_2] \quad (1)$$

In Equation (1),  $R_\psi = \psi - \psi_{LP}$  is the phase roughness, calculated from  $\psi$  by subtracting its low-pass-filtered version,  $\psi_{LP}$ ,  $S$  is the binary object support (i.e., the mask), and  $S_2 = (F_S || S_{(\psi>0)})$  is the result of the logical or between the support frontier  $F_S$  and the binary map,  $S_{(\psi>0)}$ , obtainable by segmenting  $\psi$  using a zero threshold. The stack  $\Sigma$  is sufficient to provide a complete characterization of the objects through the set of features extracted from it. Table S1, Supporting Information, summarizes the descriptors we used to train the SVM and the element of  $\Sigma$  from which each of them is calculated. A short description of each of them is also provided. The element  $\psi$  allows calculating the most common texture-based parameters that are widely used in the image processing framework. In addition, four parameters

are trivially obtainable from the roughness map,  $R_\psi$ . Morphological properties based on the object support, e.g., the area, perimeter, eccentricity, length, and breadth of the bounding box, are obtained from  $S$ . The number of vertexes of the bounding box is in principle a good identifier of MPs with very irregular silhouettes in the hologram plane, as natural water samples tend to be more regularly shaped. However, due the wide variety of diatom populations present in water samples, this feature alone would not be sufficient to guarantee high classification accuracy, so the dimensionality of the descriptor space needs to be extended. In addition to these parameters, we included new features that have been conceived to measure the spatial density of the phase jumps and, in general, the attitude of the support  $S_2$  to occupy a 2D space. Similarly to fractal objects with fractal dimension lower than 2, we note that the map  $S_2$  obtained from an MP sample tends not to completely fill the 2D domain included inside  $S$ . Thus, we also calculate the object solidity and define three new features, namely, the fill ratio,  $F_R$ , the support fractality,  $S_{Fr}$ , and the total variation density,  $TV_D$ , as

$$F_R = \frac{A\{S\}}{A\{S_2\}}; S_{Fr} = 1 - \frac{P\{S\}}{P\{S_2\}}; TV_D = \frac{TV\{\psi \odot S\}}{A\{S\}} \quad (2)$$

where we denote with  $A\{\dots\}$  and  $P\{\dots\}$  the operators that measure the area and perimeter, respectively,  $TV\{\dots\}$  follows the common definition of total variation, and  $\odot$  is the element-wise product.

As a guide criterion for the selection of the descriptors constituting the parameter space, we used the Pearson correlation matrix analysis<sup>[38]</sup> to discard parameters that would have provided redundant dimensions. Following this criterion, we based the SVM on a 28-dimension space, whose features are listed in Table S1, Supporting Information, and represented by the matrices in **Figure 3b,c**. The Pearson matrix itself can be thought as a marker of a specific class of objects. Indeed, in **Figure 3c**, the Pearson matrices obtained by nine different diatom populations are well distinguishable by the matrix calculated from the MP training set (**Figure 3b**), as detailed in the following.

## 2.3. New Informative Features from DH Data

First, we selected the 19 most used descriptors related to morphology and texture of the imaged objects, typically used in image classification by ML<sup>[38,39]</sup> (see the Supporting Information for a comprehensive description of the proposed set). A synthetic statistical representation that describes how much a set is able to separate one population from the others is provided by the Pearson correlation coefficients matrix, which measures the mutual correlation among features.<sup>[40]</sup> The higher the correlation between two features, the higher the redundancy introduced by the use of both of them. In other words, the optimality of a set of descriptors is strictly related to the minimization of their mutual correlations. The Pearson matrices corresponding to the diatoms show in some cases a significant decorrelation between the features, thus suggesting that these could be informative enough to characterize some DS (see the red boxes in **Figure 3c**). However, by evaluating the section of Pearson matrices corresponding to the sole selected 19 descriptors in the MP case, we can notice that some of them are highly correlated with

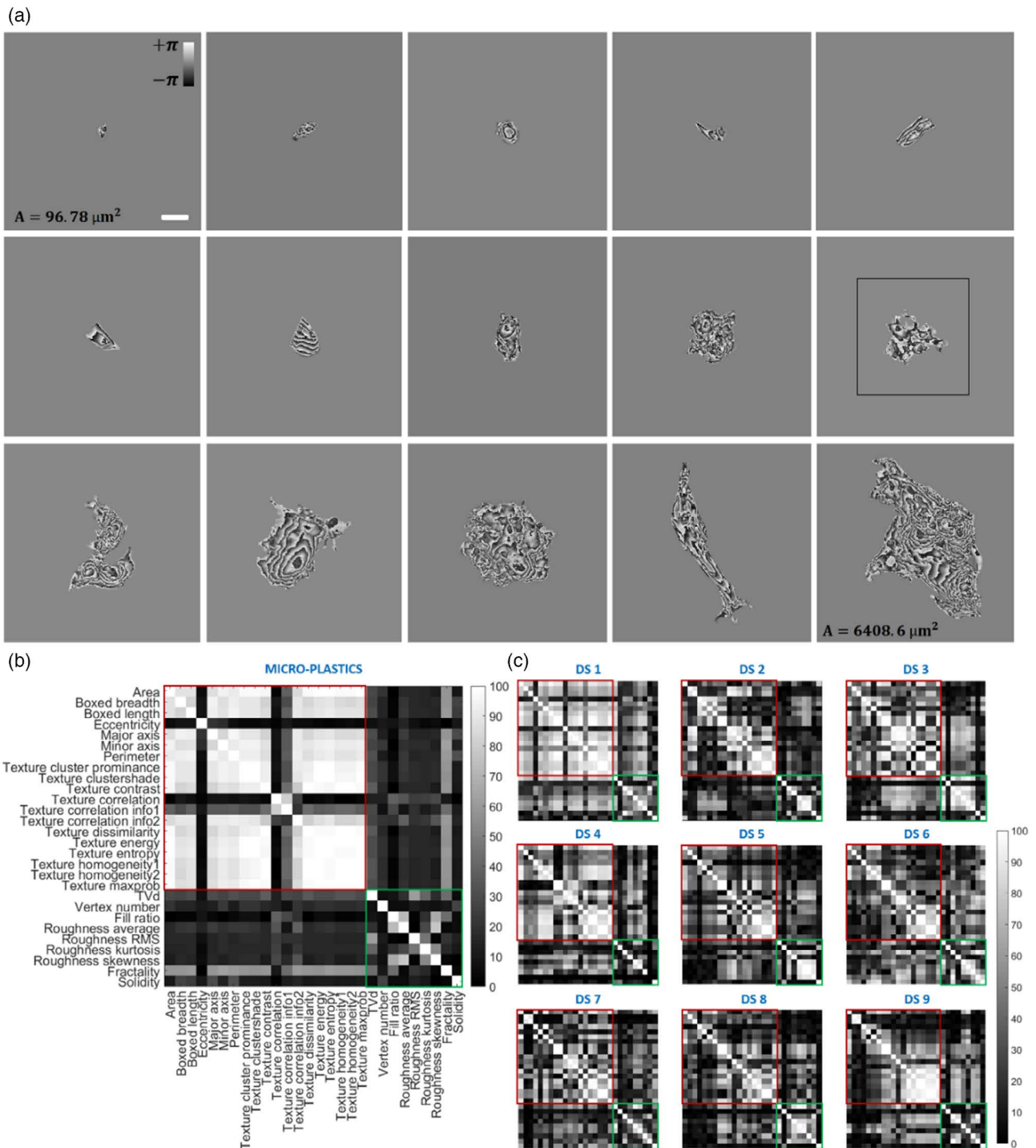


**Figure 3.** Holographic characterization of MPs. a) Examples of wrapped phase images of MPs sorted by area (from top left to bottom right), highlighting the random spreading of their sizes, shapes, and phase jumps (scale bar: 20  $\mu\text{m}$ ). b) Pearson correlation matrices calculated for the MP and the diatom classes using the complete set of the 28 proposed descriptors. The red and green boxes correspond to the Pearson matrices obtainable from the sole classical and holographic feature sets, respectively.

each other (see the red box in Figure 3b), thus suggesting the nonoptimality of this feature set for the purpose of MP classification. Consequently, we designed a new set of nine descriptors based on the holographic nature of the phase images of MPs. By

adding them to the previous 19 ones, we can define new Pearson correlation coefficient matrices that provide a more accurate representation of the samples (see green boxes in Figure 3b,c). The new set is tailored to identify MPs with high accuracy and the

HPI works well in the presence of different MP materials of various morphologies and characteristic scales. Introducing parameters measured from phase-contrast maps allows enlarging the dimensionality of the conventionally used classification space by adding new basis vectors, thus creating the conditions to separate the populations through a trained SVM. Indeed, by inspecting the entire Pearson matrix in Figure 3b, the significant degree of decorrelation of the added features, among each other (see the green box area in Figure 3b) and, above all, with respect to the classical set (see the areas outside both the green and the red boxes in Figure 3b), is evident. To quantify such decorrelation, we calculated the average value of mutual correlation in the areas highlighted with the red and green boxes of the Pearson matrices in Figure 3b,c and over the entire Pearson matrix. As the ideal condition would be to have descriptors generating an identity Pearson matrix, i.e., minimizing the mutual correlation, we quantified the decorrelation using the root mean square error (RMSE) estimator

$$\text{RMSE}_{\text{Pearson}-c} = \sqrt{\langle |\mathbf{P}_c - \mathbf{I}|^2 \rangle_B} \quad (3)$$

where  $\mathbf{P}$  is the Pearson matrix,  $\langle \dots \rangle$  is the expectation operator,  $c = 1, \dots, 10$  denotes the class,  $B$  denotes the box, and  $\mathbf{I}$  is the identity matrix. The results of such analysis (see Figure S1, Supporting Information) show that the RMSE corresponding to the classical descriptors (including morphological and texture information) stays above 78% for the MP class, whereas the RMSE between the holographic features for the same class is below 31%. By measuring the average value of mutual correlation over the yellow box in Figure S1, Supporting Information, it is possible to assess how much the new holographic descriptors are correlated to the classical ones, i.e., how informative the new set is. It is interesting to note that the mutual correlation between new and classical features stays below 26% when these are applied to MP items, suggesting the possibility to enrich the classical set with new information. The correlation difference between the red and green areas of the MP Pearson matrix is the largest among the ten classes. Moreover, the yellow bar in Figure S1, Supporting Information, is the lowest among the classes (with the sole exception of DS5), thus confirming that the new feature set is highly discriminative for the MP population. Nevertheless, the blue bar (denoting the complete set of descriptors) shows a decrease in the RMSE for all ten classes with respect to the classical set (red bar), suggesting that the new set may be able to improve the overall classification performance. The analysis of the Pearson matrices is a first clue of the advantage deriving from the introduction of nonredundant information content for this specific recognition problem.

### 3. Results

To measure the discriminative power of the set of features for MP identification, we solve a classification problem. To this aim, we use the H-SVM and we carry out  $K$ -folding cross-validation tests.<sup>[29]</sup> We captured holograms of liquid samples (i.e., sterile seawater; see Supporting Information) containing homogenous populations; i.e., each of the ten classes of objects was sampled separately through the holographic system. Thus,

for each of the reconstructed objects, a labeling indicating the belonging class was available. We exploited this information for both training and validation purposes.

#### 3.1. Holographic Support Vector Machine

From the acquired sequences of reconstructed holograms, we identified a total of  $N = 2000$  objects evenly distributed among the ten classes. For each object, we calculated the stack of maps from which the set of 28 features has been extracted and used to classify through the SVM. At the scope of studying the effect of the introduction of the new distinctive descriptors based on the wrapped phase map, we repeated the test by removing them and maintaining only the 19 “classical” ones used for object classification.<sup>[38]</sup> We will hereafter refer to this choice as “C-SVM.” The classifier performance metrics were measured in both cases. The  $K$ -folding tests were repeated varying the  $K$ -folding factor,  $K = \{5, 10, 20\}$ . Once the parameter  $K$  is set,  $N$  is divided in  $K$  balanced subsets;  $K - 1$  subsets are used to train the SVM, and the one out of  $K - 1$  subsets is used for validation. Thus, the number of objects used for training and validation,  $T_K$  and  $V_K$ , respectively, is set as well. When  $K = 5$ , the set  $N$  is divided in  $K$  groups so that  $T_5 = 1600$  and  $V_5 = 400$ . Similarly, when  $K = 10$ , we have  $T_{10} = 1800$  training objects and  $V_{10} = 200$  validation objects, while with  $K = 20$  it follows  $T_{20} = 1900$  and  $V_{20} = 100$ . For each value of  $K$ , classification was performed, and the confusion matrix was extracted, from which we calculated the performance metrics. We repeated this classification process  $M = 5000$  times. Then we calculated average values for each metric and the corresponding uncertainty. In the case of metrics indirectly measured from the values directly available from the confusion matrix, the propagation of uncertainties rule was followed. The estimated performance metrics of the classifier are shown in Figure S3a–d, Supporting Information, and summarized in Table 1. In particular, from the first row of Table 1, it can be observed that the H-SVM is able to classify the ten populations with accuracy up to  $99.31\% \pm 0.19\%$ , whereas the accuracy obtainable by C-SVM can drop below 88% with a larger uncertainty (up to 0.62%). Figure S3a–d, Supporting Information, compares the H-SVM and the C-SVM in terms of the main performance metrics measured for different values of  $K$ , namely, precision, specificity, sensitivity, and  $F_1$  score.<sup>[41]</sup> The H-SVM is estimated to classify with precision up to  $99.10\% \pm 0.41\%$  (see Figure S3a, Supporting Information). Remarkably, the precision reduces up to  $60.07\% \pm 0.58\%$  if the C-SVM is used, i.e.; the gain in precision obtained adding the new holographic set approaches 40%. Similarly, the classifier sensitivity is higher than 96.7% if the complete set of features is used, whereas it drops down to  $90.78\% \pm 0.64\%$  in the case of C-SVM (Figure S3b, Supporting Information). The specificity of the classifier is estimated to range between 99.8% and 99.9%, as shown in the plots of Figure S3c, Supporting Information, and shown in Table 1. The  $F_1$  score, which is an average measure of precision and recall, reaches the estimated value of  $97.61\% \pm 0.41\%$  for  $K = 10$  when the H-SVM is used, while it lowers to  $72.92\% \pm 0.38\%$  when the sole conventional features are used; i.e., a 25% gain in  $F_1$  score is obtained (Figure S3d,

**Table 1.** Classifier performance. Comparison between C-SVM (gray shading) and H-SVM (no shading) in terms of the main performance metrics, measured for different values of  $K$ . The performance gains for each metric are also reported. The most remarkable results are highlighted by red color.

	$K = 5$		$K = 10$		$K = 20$	
Accuracy [%]	99.13 ± 0.23	+11.90%	99.26 ± 0.20	+11.56%	99.31 ± 0.19	+11.43%
	87.23 ± 0.58		87.70 ± 0.61		87.88 ± 0.62	
Precision [%]	98.36 ± 0.69	+38.29%	98.84 ± 0.51	+38.02%	99.10 ± 0.41	+37.94%
	60.07 ± 0.58		60.82 ± 0.46		61.16 ± 0.41	
Sensitivity [%]	95.70 ± 0.86	+4.92%	96.40 ± 0.64	+5.39%	96.72 ± 0.47	+5.56%
	90.78 ± 0.64		91.01 ± 0.52		91.16 ± 0.43	
Specificity [%]	99.82 ± 0.08	+6.53%	99.87 ± 0.05	+6.38%	99.90 ± 0.04	+6.33%
	93.29 ± 0.14		93.49 ± 0.11		93.57 ± 0.10	
$F_1$ Score [%]	97.01 ± 0.56	+24.71%	97.61 ± 0.41	+24.69%	97.89 ± 0.32	+24.68%
	72.30 ± 0.47		72.92 ± 0.38		73.21 ± 0.33	

Supporting Information). The four plots show also a small variance over the metrics on the various  $K$ -folding as the average on the 5000 trials. The benefit of the holographic descriptors is evident along all the metrics, and the variance of the sensitivity is wider due to MPs' higher variability. The sensitivity of the tested classifier has higher values due to its capabilities in correctly classifying the true positive rates. These results show the effectiveness of the HPI in identifying plastic items spanning over a wide range of scales and with large variability of shapes and material types, when these have to be recognized inside a heterogeneous mixture, e.g., in a microfluidic flow.

After validating the classifier performance, we conducted a new campaign of experiments and we used it to classify objects belonging to the ten populations from a wider set of samples. In particular, we identified hundreds of objects per class and a total of  $T = 10\,000$  elements, evenly distributed among the ten classes (i.e., 1000 training elements per class), was obtained by data augmentation. Then, in a subsequent set of acquisitions, we captured with the same setup holograms of liquid volumes from which we identified a total of  $V = 500$  validation objects evenly distributed among the populations. We trained the SVM using the features extracted from the  $T$  objects and used it to measure the rate of correct detections from the data of the  $V$  objects acquired in the second experiment. The correct detection rate is measured as the ratio between the true positives and the total number of validation objects,  $V$ , resulting in 99.8% of correct detections. If the complete holographic set is used as the input of a linear classifier, this can discriminate between the ten populations with 98.2% of accuracy. When we used a 19-feature subspace that did not include the highly distinctive basis components, the accuracy of the classifier approached only 81%; i.e., the linear classifier gained 17% in accuracy. In other words, the HPI embedding a linear classifier enriched by holographic descriptors outperformed the C-SVM in terms of classification accuracy. Above all, if the H-SVM is thought of as a binary MP identifier taking a yes/no decision between plastic items and diatoms (i.e., without including classification among the DS), the accuracy value reaches 100%, with no false positives

(FPs) and no false negatives (FNs). At first analysis, these results could be considered somehow expected due to the larger dimensionality of the 28-feature space with respect to the 19-feature space of conventional descriptors. Thus, we conducted a further assessment test using the linear classifier as a benchmark. In particular, we compared the classification performance we obtained using the same linear classifier when this takes decisions based on the 19 conventional descriptors and the sole nine new features we introduced. Contrary to expectations, the linear classifier based on the lower dimensionality space was 84.6% accurate, i.e., 3.2% better than the classifier working on a significantly larger dimensionality space. Only a 2.6% classification error was associated with the MP class, whereas this value approached 10% when the larger but less distinctive set of conventional features was used. These results prove the effectiveness of the holographic approach proposed here as an optical marker for the MP class. To show the advantage of adopting the proposed approach in the case of a reduced number of data available for training, in the Supporting Information we report a comparison between the obtained performance and the results obtainable using a well-established deep neural network architecture.<sup>[42]</sup>

### 3.2. Solving Misclassifications

To show how the stack  $\Sigma$  allows for solving ambiguities between "similar" populations, in **Figure 4** we report two examples of binary classification between MPs and diatoms with comparable morphologies and sizes. In particular, **Figure 4a** shows the maps  $\psi$ ,  $S$ , and  $S_2$  obtained from one of the MPs (top row) and one of the elements of the population DS3 (bottom row). In this case, the two objects have similar morphological characteristics, e.g., in terms of area, perimeter, or eccentricity, so C-SVM is likely to fail in discerning between them. To have an indication of the frequency of this type of error, we extracted from the  $K$ -folding tests the sole elements describing a binary classifier devoted to discern between MPs and DS3. The table in **Figure 4b** shows the results obtained in the case  $K = 5$ . The number of FNs and FPs has been calculated from the confusion matrix obtained after averaging the set of  $T = 5000$  confusion matrices estimated during the  $K$ -folding tests. Results indicate that the sole class DS3 generates 20% of FPs and a few FNs, meaning that MPs would be overestimated in the presence of small-sized algae. However, when we introduce the new parameters devoted to assess the capability of  $S_2$  to fill a 2D space and the irregularities of its silhouette, both the FN and FP percentages drop to zero; i.e., all the  $2L = 400$  objects are correctly classified. Indeed, the maps  $S_2$  in the top and bottom row of **Figure 4a** do not fill their own supports to the same extent, and the new features are sensitive to this difference. A similar comparison is shown in **Figure 4c,d**, where we show the performance of a binary classifier devoted to discern between plastic items and objects belonging to the population DS1. In particular, the example reported in **Figure 4c** shows the case of an MP that has been classified as a DS1 through the use of the C-SVM. Instead, this is correctly classified when the H-SVM is used. The table in **Figure 4d** shows that the sole class DS1 would generate 28% of FPs and 3.5% of FNs. However, the H-SVM is almost error free in this case, with 0% of FPs and 0.5% of FNs. This explains the increase of specificity and sensitivity

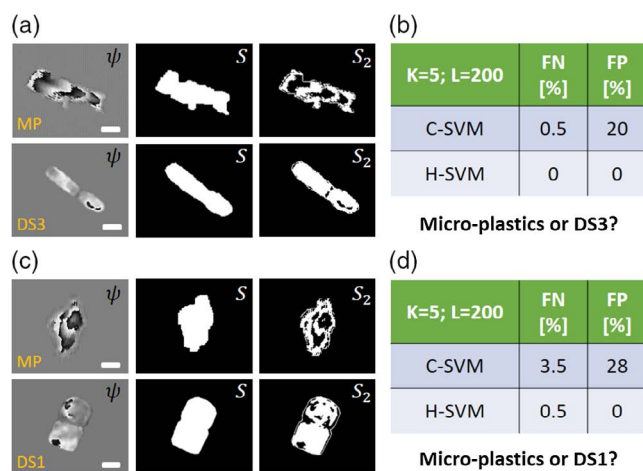


**Figure 4.** FP and FN test cases. a,c) Two examples of how the SVM classifier based on the sole classical features (C-SVM) confuses DS with MPs (FPs) and vice versa (FNs). Examples of MPs (first row) and DS (second row) are reported, as seen through the maps  $\psi$ ,  $S$ , and  $S_2$ . The sole use of  $S$  is clearly not sufficient to discern between these populations, which is the reason for the large FP percentages obtained by the C-SVM. (Scale bar: 5  $\mu\text{m}$ .) b,d) Tables that summarize the FP and FN percentage count in the cases of C-SVM and H-SVM. The H-SVM is error free in terms of FPs.

(FPs are reduced to zero being in the denominator of the two metrics) and strongly supports the power of the descriptors in correctly rejecting hypothesis of being MPs when the true state of nature is a diatom and vice versa.

#### 4. Discussion and Conclusions

We introduced an automatic prescreening approach that enables accurate and automatic detection of MPs in pretreated water samples over a wide range of scales by combining 3D coherent imaging with ML. Results show that ML based on an optimal set of holographic features improves MP recognition in heterogeneous samples. We achieved over 99% of accuracy in classifying ten populations, including nine DS and a MP mixture including several different plastic materials. Residual classification errors during the test step are due to the sole misclassifications among diatom classes; i.e., no MP is classified as a DS and vice versa. In other words, considering the proposed H-SVM as a binary classifier, we are able to identify exactly MPs in pretreated seawater, thus discarding the other objects falling within the same range of characteristic scales. Previous works have proposed the use of holographic reconstructions to classify particles, cells, or microorganisms based on statistical methods or ML architectures.<sup>[43–51]</sup> However, none of the existing ML-DH approaches have tackled the problem of identifying MPs, which have their own specificity as the MP class consists of a wide heterogeneity of materials, morphologies, and characteristic scales. To the best of our knowledge, this is the first characterization of MPs based on their diffracted wavefront signature, and thus for the first time a set of holography-based features is defined to identify this very complex class of inert micro-objects. We believe this novelty can pave the way to new possibilities, allowing us to solve different classification tasks characteristic of other fields of research.

The reported results confirm that quantitative phase imaging (QPI)-DH is a very appropriate microscopy tool for addressing MPs' recognition problem, as it can guarantee quantitative 3D imaging capabilities and can analyze the content of microfluidic flows with high volumetric throughput.<sup>[20,21,52]</sup> The proposed classification approach can be of help to screen the content of seawater that previously underwent a pretreatment procedure, e.g., sieving or filtration, with the aim to identify MPs with high throughput, avoiding the use of unaided visual analysis by experts under the optical microscope. Once classification is performed, further spectroscopy-based analysis could be used only on the prescreened portion of items classified as a plastic to estimate the composition of plastic pollutants in the specific water segment under test. In this sense, the method we propose can be thought as a block to be introduced in the existing water analysis chain to accelerate the identification of MPs and to base statistical analysis on a more appropriate number of samples. It is worth pointing out that the DH diffraction limit is about 200 nm for a 532 nm wavelength, whereas a typical value of spatial resolution is 0.5  $\mu\text{m}$  for DH systems. Thus, in principle, the proposed analysis range can be extended to include particles smaller than 20  $\mu\text{m}$ . A characterization of such small samples will be the object of future work from our group.

Of course, in real field-sampling campaigns aiming at detecting pollutants of marine water, we expect to find a larger heterogeneity of plankton sizing less than 1 mm, so we foresee the performance to slightly worsen with respect to the results reported earlier. However, it has been recently shown that marine algae and microplankton species of sizes ranging between 25 and about 500  $\mu\text{m}$ , when imaged through a field portable red green blue (RGB) DH microscope, mostly show regularly shaped phase maps with no jumps or with small jumps density distribution.<sup>[21]</sup> Thus, adding a larger variety of microplankton species is not expected to affect dramatically our MP recognition performance, but only diatom taxonomy results. In other words, the discriminative power of the features introduced in this study suggests robustness against the presence of a more numerous set of populations. In addition, pretreated water samples are supposed to be free from larger-sized (multicellular) algae, sand grains, etheroaggregates, and sediments larger than 1 mm. In case some of these elements are not properly filtered out by the water treatment process, the accuracy is expected to be slightly lower than the value we reported here (>99%). For example, possible sources of classification errors could be plastic beads specifically manufactured to be very regularly shaped, which could be attributed to natural objects and generate FNs. Untrained microalgae containing lipids could be incorrectly associated with the MP class, generating FPs. Moreover, future investigations will be conducted to take into account the eventual presence of quartz or other minerals after the prefiltering treatment. We believe the potential accuracy loss in such specific cases would be still acceptable in view of the possibilities the method offers, being the first able to automatically screen MPs with a high-throughput imaging method, thus replacing the burdensome, slow, and inaccurate naked-eye observation of each single micro-object.

The measured average mutual correlation among the new holographic descriptors and the classical ones supports the use of the complete set, the lowest value being obtained for



the MP class. As a further test case, we used a plain linear classifier using the complete set of descriptors. This outperformed the C-SVM in terms of classification accuracy, thus demonstrating how holographic parameters are highly discriminative in identifying the wide MP class. The complete H-SVM has shown performance comparable to well-established a deep neural network<sup>[42]</sup> in handling the classification task, requiring a negligible time for training with respect to the amount of time required to train the network (see Supporting Information). Although the convolutional neural network is expected to be more robust when adding more and more classes, this result suggests that H-SVM could replace deep learning whenever there is no possibility of collecting a large ground truth dataset for training. We expect further improvement and the capability to handle more and more inclusive and complex classification problems by replacing the SVM with better performing classifiers.<sup>[53]</sup>

A consideration about the state of the art in sensor development is due. Combining microfluidic and DH technologies to bring high-throughput holographic sensors out of the lab and outdoor and also to extreme environments has been already demonstrated.<sup>[21,22,52]</sup> Technology is mature enough and provides day by day various imaging sensors and high-throughput portable holographic flow cytometers to be deployed on the field.<sup>[21,52]</sup> Such systems can be produced at reduced costs. Therefore, it is easy to bode for the upcoming future the use of these sensors for the monitoring of marine water looking for plastic pollutants. In this sense, HPI can be thought as a block to be introduced in the existing water analysis chain. Unlocking the possibility to perform fast, high-throughput screening within a very wide (20  $\mu\text{m}$ –1 mm) analysis range could have a remarkable impact on the environmental monitoring field. Indeed, we believe the coherent optical approach we propose here is the first important step to relax the problem burden through the identification of a marker for the wide MP class, with the hope this will help in providing a deeper knowledge of the spatial concentration of MPs and the temporal distribution of their flows.<sup>[54]</sup>

## Supporting Information

Supporting Information is available from the Wiley Online Library or from the author.

## Acknowledgements

This work was supported by the MIUR project “Sistemi di Rilevamento dell’Inquinamento Marino da Plastiche e successivo recupero-riciclo” (SIRIMAP), PON ARS01\_01183. The authors thank Dr. Eugenio Rastelli (Stazione Zoologica “Anton Dohrn” and “Università Politecnica delle Marche”) for providing and manufacturing the microplastic samples. The authors also thank the “Istituto di Chimica Biomolecolare” of the Italian National Research Council (ICB-CNR) and Dr. Stefano Barone—Diatom Lab—for providing DS for the experiments.

## Conflict of Interest

The authors declare no conflict of interest.

## Keywords

detection, digital holography, environmental monitoring, machine learning, microplastics

Received: November 21, 2019  
Published online: January 13, 2020

- [1] J. R. Jambeck, R. Geyer, C. Wilcox, T. R. Siegler, M. Perryman, A. Andrady, R. Narayan, K. L. Law, *Science* **2015**, *347*, 768.
- [2] T. S. Galloway, C. N. Lewis, *Proc. Natl. Acad. Sci.* **2016**, *113*, 2331.
- [3] D. Hoorweg, P. Bhada-Tata, C. Kennedy, *Nature* **2013**, *502*, 615.
- [4] V. Hidalgo-Ruz, L. Gutow, R. C. Thompson, M. Thiel, *Environ. Sci. Technol.* **2012**, *46*, 3060.
- [5] J. Sun, X. Dai, Q. Wang, M. C. M. van Loosdrecht, B. Ni, *Water Res.* **2019**, *152*, 21.
- [6] J. Talvitie, A. Mikola, A. Koistinen, O. Setälä, *Water Res.* **2017**, *123*, 401.
- [7] S. L. Wright, D. Rowe, R. C. Thompson, T. S. Galloway, *Curr. Biol.* **2013**, *23*, 1031.
- [8] R. Sussarellu, M. Suquet, Y. Thomas, C. Lambert, C. Fabioux, M. E. J. Pernet, N. Le Goïc, V. Quillien, C. Mingant, Y. Epelboin, C. Corporeau, J. Guyomarch, J. Robbins, I. Paul-Pont, P. Soudant, A. Huvet, *Proc. Natl. Acad. Sci.* **2016**, *113*, 2430.
- [9] C. M. Rochman, E. Hoh, T. Kurobe, S. J. The, *Nat. Sci. Rep.* **2013**, *3*, 3263.
- [10] C. M. Rochman, M. A. Browne, *Nature* **2013**, *494*, 169.
- [11] A. A. Koelmans, N. H. Mohamed Nor, E. Hermsen, M. Kooi, S. M. Mintenig, J. De France, *Water Res.* **2019**, *155*, 410.
- [12] D. Eerkes-Medrano, R. C. Thompson, D. C. Aldridge, *Water Res.* **2015**, *75*, 63.
- [13] M. Haward, *Nat. Commun.* **2018**, *9*, 1.
- [14] W. J. Shim, S. H. Hong, S. E. Eo, *Anal. Methods* **2017**, *9*, 1384.
- [15] C. F. Araujo, M. M. Nolasco, A. M. P. Ribeiro, P. J. A. Ribeiro-Claro, *Water Res.* **2018**, *142*, 426.
- [16] R. Gillibert, G. Balakrishnan, Q. Deshoules, M. Tardivel, A. Magazzù, M. Donato, O. Maragò, M. L. De la Chapelle, F. Colas, F. Lagarde, P. Gucciardi, *Environ. Sci. Technol.* **2019**, *531*, 59003.
- [17] Y. K. Song, S. H. Hong, M. Jang, J. Kang, O. Y. Kwon, G. M. Han, W. J. Shim, *Environ. Sci. Technol.* **2014**, *48*, 9014.
- [18] S. Zhao, M. Danley, J. E. Ward, D. Li, T. J. Mincer, *Anal. Methods* **2017**, *9*, 1470.
- [19] F. Merola, P. Memmolo, V. Bianco, M. Paturzo, M. G. Mazzocchi, P. Ferraro, *EPJ Plus* **2018**, *133*, 350.
- [20] L. A. Philips, D. B. Ruffner, F. C. Cheong, J. M. Blusewicz, P. Kasimbeg, B. Waisi, J. R. McCutcheon, D. G. Grier, *Water Res.* **2017**, *122*, 431.
- [21] Z. Göröcs, M. Tamamitsu, V. Bianco, P. Wolf, S. Roy, K. Shindo, K. Yann, Y. Wu, H. C. Koydemir, Y. Rivenson, A. Ozcan, *Light Sci. Appl.* **2018**, *7*, 66.
- [22] J. Watson, N. M. Burns, *Subsea Optics and Imaging* (Eds: J. Watson, O. Zielinski), Woodhead Publishing, Sawston, UK **2013**.
- [23] N. Cristianini, J. Shawe-Taylor, *An Introduction to Support Vector Machines and Other Kernel-Based Learning Methods*, Cambridge University Press, Cambridge **2000**.
- [24] A. Mahjoubfar, C. L. Chen, B. Jalali, *Artificial Intelligence in Label-Free Microscopy*, Springer International Publishing AG, New York **2017**.
- [25] A. Yevick, M. Hannel, D. G. Grier, *Opt. Express* **2014**, *22*, 26884.
- [26] B. Schneider, J. Dambre, P. Biestman, *Appl. Opt.* **2016**, *55*, 133.
- [27] Y. LeCun, Y. Bengio, G. Hinton, *Nature* **2015**, *521*, 436.
- [28] Y. D. Bedoshvili, T. P. Popkova, Y. V. Likhoshway, *Cell Tissue Biol.* **2009**, *3*, 297.
- [29] C. M. Bishop, *Pattern Recognition and Machine Learning*, Springer-Verlag New York, New York **2006**.

- [30] P. Memmolo, L. Miccio, M. Paturzo, G. Di Caprio, G. Coppola, P. A. Netti, P. Ferraro, *Adv. Opt. Photonics* **2015**, 7, 713.
- [31] M. Eriksen, L. C. Lebreton, H. S. Carson, M. Thiel, C. J. Moore, J. C. Borerro, F. Galgani, P. G. Ryan, J. Reisser, *PLoS One* **2014**, 9, e111913.
- [32] L. S. Fendall, M. A. Sewell, *Mar. Pollut. Bull.* **2009**, 58, 1225.
- [33] P. Memmolo, V. Bianco, M. Paturzo, P. Ferraro, *Proc. IEEE* **2017**, 105, 892.
- [34] Y. Zhang, H. Wang, Y. Wu, M. Tamamitsu, A. Ozcan, *Opt. Lett.* **2017**, 42, 3824.
- [35] J. M. Bioucas-Dias, G. Valadão, *IEEE Trans. Image Process.* **2007**, 16, 698.
- [36] Scientific Polymer Products, Inc. homepage, <https://scientificpolymer.com/technical-library/refractive-index-of-polymers-by-index/> (accessed: September 2019).
- [37] M. Ferrara, P. Dardano, L. De Stefano, I. Rea, G. Coppola, I. Rendina, R. Congestri, A. Antonucci, M. De Stefano, E. De Tommasi, *PLoS One* **2014**, 9, e103750.
- [38] M. Hejna, A. Jorapur, J. S. Song, R. L. Judson, *Sci. Rep.* **2017**, 7, 11943.
- [39] R. M. Haralick, K. Shanmugam, I. Dinstein, *IEEE Trans. Syst. Man Cybern. SMC* **1973**, 3, 610.
- [40] K. Pearson, *Proc. R. Soc. Lond.* **1895**, 58, 240.
- [41] D. M. W. Powers, *J. Mach. Learn. Technol.* **2011**, 2, 37.
- [42] Y. Lecun, L. Bottou, Y. Bengio, P. Haffner, *Proc. IEEE* **1998**, 86, 2278.
- [43] B. Javidi, I. Moon, S. Yeom, E. Carapezza, *Opt. Express* **2005**, 13, 4492.
- [44] I. Moon, B. Javidi, *J. Biomed. Opt.* **2006**, 11, 064004.
- [45] Y. Jo, S. Park, J. Jung, J. Yoon, H. Joo, M. Kim, S. Kang, M. Choi, S. Lee, Y. Park, *Sci. Adv.* **2017**, 3, e1700606.
- [46] M. Rubin, O. Stein, N. A. Turko, Y. Nygate, D. Roitshtain, L. Karako, I. Barnea, R. Giryas, N. T. Shaked, *Med. Image Anal.* **2019**, 57, 176.
- [47] S. J. Kim, C. Wang, B. Zhao, H. Im, J. Min, H. J. Choi, J. Tadros, N. R. Choi, C. M. Castro, R. Weissleder, H. Lee, K. Lee, *Sci. Rep.* **2018**, 8, 17003.
- [48] H. S. Park, M. T. Rinehart, K. A. Walzer, J. T. A. Chi, A. Wax, *PLoS One* **2016**, 11, e0163045.
- [49] Y. Jo, H. Cho, S. Y. Lee, G. Choi, G. Kim, H. Min, Y. Park, *IEEE J. Sel. Top. Quantum Electron.* **2018**, 25, 1.
- [50] S. K. Mirsky, I. Barnea, M. Levi, H. Greenspan, N. T. Shaked, *Cytom. A* **2017**, 91, 893.
- [51] C. L. Chen, A. Mahjoubfar, L. Tai, I. K. Blaby, A. Huang, K. R. Niazi, B. Jalali, *Sci. Rep.* **2016**, 6, 21471.
- [52] B. Mandracchia, V. Bianco, Z. Wang, M. Mugnano, A. Bramanti, M. Paturzo, P. Ferraro, *Lab Chip* **2017**, 17, 2831.
- [53] T. Chen, C. Guestrin, KDD '16 Proc. 22nd ACM SIGKDD International Conf. on Knowledge Discovery and Data Mining, San Francisco, CA, August 13–17, **2016**, pp. 785–794
- [54] Editorial, *Nat. Commun.* **2018**, 9, 2157, <https://doi.org/10.1038/s41467-018-04565-2>.